ARTICLE

FePd nanowires modified with cyclodextrin as improved catalysts: Effect of the alloy composition on colloidal stability and catalytic capacity.

Elisa Herrera,[a,b] Julieta Riva,[c] Soledad Aprea,[c,d] O. Fernando Silva,[a,e] Paula G. Bercoff [c,d] and Alejandro M. Granados*[a,e]

In the present work, FePd nanowires of different compositions, namely $Fe_{85}Pd_{15}$, $Fe_{65}Pd_{35}$, $Fe_{55}Pd_{45}$ and Fe_0Pd_{100}, were synthesized by electrodeposition into the nanopores of alumina membranes. The samples were characterized by XRD, SEM, EDS, XPS, and magnetometry. The surface of the nanowires was functionalized with a cyclodextrin derivative (βCDMOD14) to obtain stable aqueous dispersions. A comprehensive study about the relationship between the alloy composition and the catalytic capacity of FePd nanowires (FePdNWs) modified with βCDMOD14 was conducted through the analysis of the rate constants (k_{obs}) of the reduction reaction of 4-nitrophenol to 4-aminophenol with sodium borohydride mediated by the FePdNWs in water. The highest value of k_{obs} was observed for $Fe_{55}Pd_{45}$ NWs, but the catalytic performance of $Fe_{65}Pd_{35}$ NWs was similar to the previous one, in spite of its lower Pd content. The presence of Fe atoms and the synthesis method promotes the formation of an *fcc* phase in the alloy, which shows higher catalytic activity than pure Pd, possibly because of a synergistic effect exerted by Fe. The catalysts can be easily recovered by taking advantage of their magnetic properties to be reused after reactivation with βCDMOD14.

Introduction

The catalytic capacity of Pd has been widely demonstrated and this element has been was successfully employed as a catalyst in chemical reactions which involve hydrogen or oxygen release. In that sense, there is evidence that Pd is able to store these atoms due to the nature of its crystalline structure.[1–8] As a consequence of the high surface/volume ratio that nanoparticles (NP) and nanowires (NWs) exhibit,[4,9] Pd nanostructures would appear as excellent materials for their use as catalysts.[10] However, because of the aforementioned advantages, in the last decades, the increasing interest in palladium was also accompanied by a price rise.[1–5,10,11] Additionally, the environmental and human health damage related to its accumulation is still not well-known.[12,13] So, the study of nanocatalysts in which Pd is combined with other compounds such as metals, non-metals, oxides, organic molecules, or composites is interesting, in order to decrease the amount of Pd used in the catalyst. Furthermore, if possible, the designed nanocatalyst should be recoverable for reuse by applying a simple procedure.[6,14] Several combinations of metals have been used to synthesize nanoparticles in which a magnetic element is present so that they can be easily recovered from the reaction medium after the catalysis reaction occurs, thereby simplifying the stage of separating the catalyst from the reaction product.[14–18] Also, in some cases, a synergistic effect between Pd and the magnetic metals has been postulated. That behavior was firstly observed and reported for Pt-M NP (where M is a transition metal) by Stamenkovic et al. who showed that PtNi NP were 10 times more active for oxygen reduction reaction (ORR) than pure Pt NP, also increasing the stability of the catalyst.[1] Liu et.al. studied the effect of overlapping FePd sheets on a top layer of pure Pd in the ORR and they found that the catalytic activity was increased and the lattice parameters of Pd were modified as a result of the presence of the FePd alloy.[19] Additionally, Jiang et. al. evaluated the catalytic activity of FePd@Pd core/shell NP, finding that it increased as the shell thickness increased up to a critical value, over which the influence of the core was weak and the catalytic activity decreased.[20,21]

In order to obtain an optimal catalyst, several characteristics of the material are relevant such as its morphology and crystallinity, as well as the composition. Therefore, a complete characterization is crucial in the process for selecting the catalyst because it enables determining the appropriate

a. *Universidad Nacional de Córdoba. Facultad de Ciencias Químicas. Departamento de Química Orgánica. Córdoba, Argentina.*

b. *Consejo Nacional de Investigaciones Científicas y Técnicas, CONICET. Instituto Nacional del Agua, Subgerencia Centro de la Región Semiárida (INA-SCIRSA). Córdoba, Argentina.*

c. *Universidad Nacional de Córdoba. Facultad de Matemática, Astronomía, Física y Computación.*

d. *Instituto de Física Enrique Gaviola, IFEG. Consejo Nacional de Investigaciones Científicas y Técnicas, CONICET. Córdoba, Argentina.*

e. *Consejo Nacional de Investigaciones Científicas y Técnicas, CONICET. Instituto de Investigaciones en Fisicoquímica de Córdoba, INFIQC. Córdoba, Argentina.*

synthesis parameters, which generally control the catalytic behavior of the nanostructures[1,2,19,20]. In the previously mentioned reports, Stamenkovic et al. studied bimetallic Pt_3Ni NP and found that (111) crystalline planes are considerably more active in ORR than the low-index planes (100) and (110).[1] These differences in catalytic activity between different phases have also been observed in FePd alloys, whose superficial layer's crystalline phase might be determinant in the resulting catalytic properties. In any case, as far as we have been able to compare, this capacity is always greater for the alloy than for pure Pd.[22–25] One of the key factors for the formation of the adequate crystalline phases that promote catalysis in a desired nanostructure is the material's synthesis process. In that sense, electrodeposition into the nanopores of ordered anodic aluminum oxide is a low-cost technique that may also facilitate the formation of the desired crystalline phases of the electrodeposited materials.[26,27]

One of the aims of this work is to obtain a nanocatalyst for uses in aqueous media. However, it is widely known that the metallic nanostructures coalesce in this condition. In order to avoid that undesirable effect, which decreases the active surface in the catalyst, a stabilizer such as Cyclodextrins (CDs) can be added on the surface of the nanostructure.[28–30] CDs are macrocyclic compounds formed by α-D-glucopiranose units bonded by α-1,4-glycosidic bonds which have a hydrophobic internal cavity and a hydrophilic external surface; they are an accessible and non-toxic alternative to other stabilizers. An additional exceptional feature is their ability to form reversible host-guest complexes with particular compounds, thereby facilitating catalytic transformations.[31] CDs and their derivate are adsorbed on the surface and give excellent colloidal stability to the nanostructures. We have recently reported the remarkable effect of βCDMOD14 (see Scheme 1)[32] on the colloidal stability and catalytic activity of Pd NP (Pd NPs)[33] and $Fe_{55}Pd_{45}$ NWs ($Fe_{55}Pd_{45}$ NWs).[29]
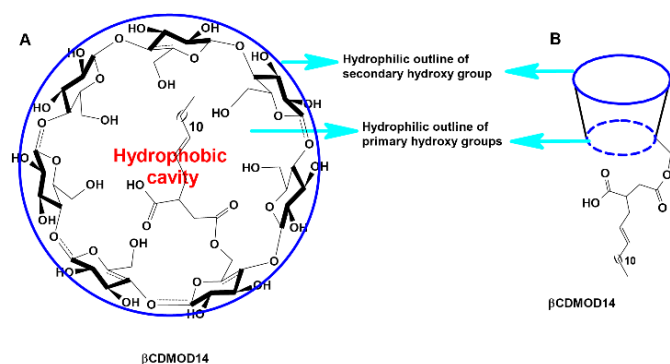
Scheme 1. **A**: Chemical structure of βCDMOD14 and its hydrophilic/hydrophobic zones. **B**: Schematic representation of βCDMOD14.

The reduction of 4-nitrophenol (4-NP) to 4-aminophenol (4-AP) has been frequently used as a model reaction in order to evaluate the catalytic activity of metal NPs due to the simple and accurate procedure for measuring the reaction progress

by UV–vis spectroscopy. Two distinct mechanisms for 4-NP reduction in presence of NPs are worth mentioning: (a) a surface-mediated electron transfer and (b) a surface-mediated hydrogen transfer. According to the postulated models, both mechanisms have the same requirement of a surface where the reduction process takes place.[34]

In this work, we estimate the threshold percentage (100-x) of Pd in $Fe_xPd_{(100-x)}$ NWs that is needed to improve the catalytic effects in the previously-mentioned reduction reaction, as an important pathway for preparation of low-cost, highly active and stable catalysts. In particular, we focus on an atomic Fe/Pd ratio higher than 1 in order to promote an efficient, easily-recovering, and economic catalyst that may reduce the environmental impact; these are additional key parameters in catalytic studies. A plausible interpretation of the βCDMOD14 coating in increasing the catalytic activity of these surfaces is also proposed, in order to deepen the knowledge about the catalytic processes. This work shows that βCDMOD14 coating plays a key role by shielding the NWs surface from aggregation and increasing the catalytic activity through the formation of inclusion complexes with 4-NP. We also propose a possible explanation of the effect that the FePd alloy composition has on the colloidal and catalytic behavior. The findings not only allow the identification of key steps involved in the catalytic reaction on the NWs surface, but also open an avenue towards the rational design of improved catalysts.

Results and Discussion

Figure 1 displays SEM images taken from the samples after partially dissolving the AAO template. The obtained NWs replicate the pores' morphology, with uniform and smooth surfaces. The difference in composition does not modify the NWs shape, being the mean length L different, depending on composition (see Table 1). As expected, the NWs diameters are approximately 200 nm, the same diameter as the pores of the alumina template.
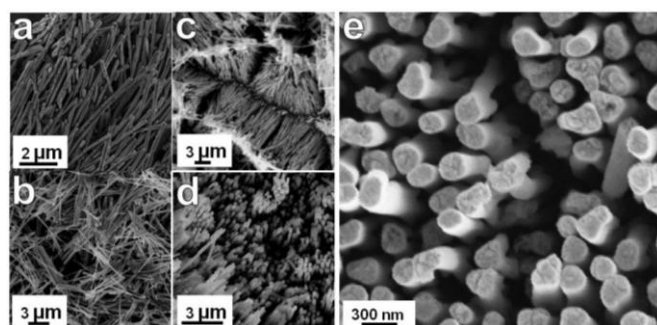
Figure 1. SEM images of different composition NWs. a) Pd b) $Fe_{55}Pd_{45}$ c) $Fe_{65}Pd_{35}$ d) and e) $Fe_{85}Pd_{15}$.

The chemical compositions were obtained by taking the average of several EDS spectra (Figure S1) measured in

different areas of each FePd NWs sample, and are listed in Table 1.

The crystalline structure of the as-electrodeposited NWs was studied by X-ray diffraction (XRD), and the X-ray diffractograms of the FePd NWs inside the AAO template are shown in Figure2.

Table 1. Fe^{3+} and Pd^{2+} concentrations of the solutions used to synthesize the NWs[a], composition in at. % of Fe^0 and Pd^0 determined by EDS[b], and length L determined by SEM images.

[Fe^{3+}] mM / [Pd^{2+}] mM[a]	Composition at%.[b]	Lenght L^c [±2 μm]
8.33 / 0.67	$Fe_{85}Pd_{15}$	8
6.67 / 1.33	$Fe_{65}Pd_{35}$	22
5.00 / 2.00	$Fe_{55}Pd_{45}$	13
0 / 4.00	Fe_0Pd_{100}	10

[c] The diameter of the NWs of all compositions was approximately 200 nm, as determined by the pore diameter of the AAO membranes.
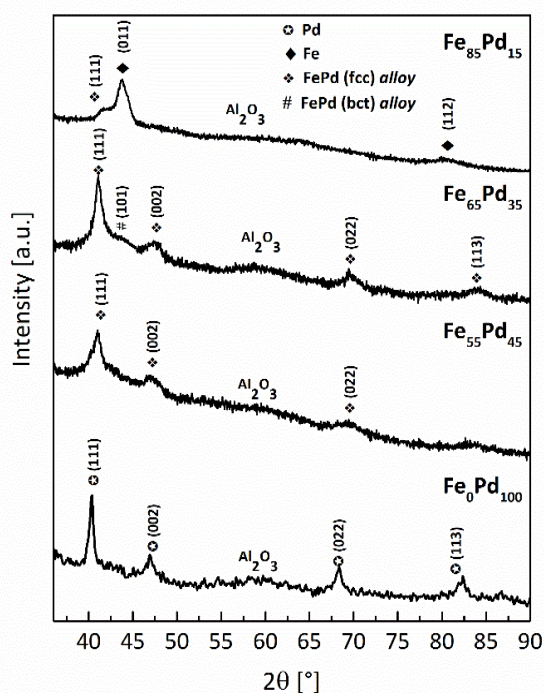
Figure 2. XRD of as-deposited $Fe_{85}Pd_{15}$, $Fe_{65}Pd_{35}$, $Fe_{55}Pd_{45}$ and Fe_0Pd_{100} NWs arrays in AAO templates of 200 nm diameter.

The as-deposited pure Pd NWs have an *fcc* structure and grow preferentially along the (022) crystal direction, which corresponds to the peak at 2θ=68.44°. For the alloyed FePd NWs, the peaks observed around 41°, 47° and 68° are associated to reflections from the (111), (002) and (022) planes of a γ-FePd disordered phase.[35] The lattice parameter a and the average crystal size d_{Sch} in each sample (calculated using the Scherrer formula), are shown in Table 2. In $Fe_{55}Pd_{45}$ and $Fe_{65}Pd_{35}$ NWs, all the observed peaks correspond to a Fe–Pd

alloy. In $Fe_{85}Pd_{15}$, the most intense peak of α-Fe corresponding to the reflection of plane (011) is also detected, which

Table2. XRD and magnetic parameters.

Samples	a [Å] FePd alloy	a [Å] Fe	d_{Sch} [nm] FePd alloy	(μ_0 Hc±2) ∥ [mT]	(μ_0 Hc±2) ⊥ [mT]	Mr ∥	Mr ⊥
$Fe_{85}Pd_{15}$	3.7746	2.9318	13±2	13	14	0.10	0.05
$Fe_{65}Pd_{35}$	3.8436		8±2	5	10	0.06	0.04
$Fe_{55}Pd_{45}$	3.8465		6±2	5	10	0.08	0.05
Fe_0Pd_{100}	3.8963		14±3				

Lattice parameter a, and crystallite size d estimated from XRD patterns. Coercive field, μ_0Hc, and relative magnetic remanence, Mr, corresponding to the external field applied, parallel (∥) and perpendicular (⊥) to the NWs long axis are shown.
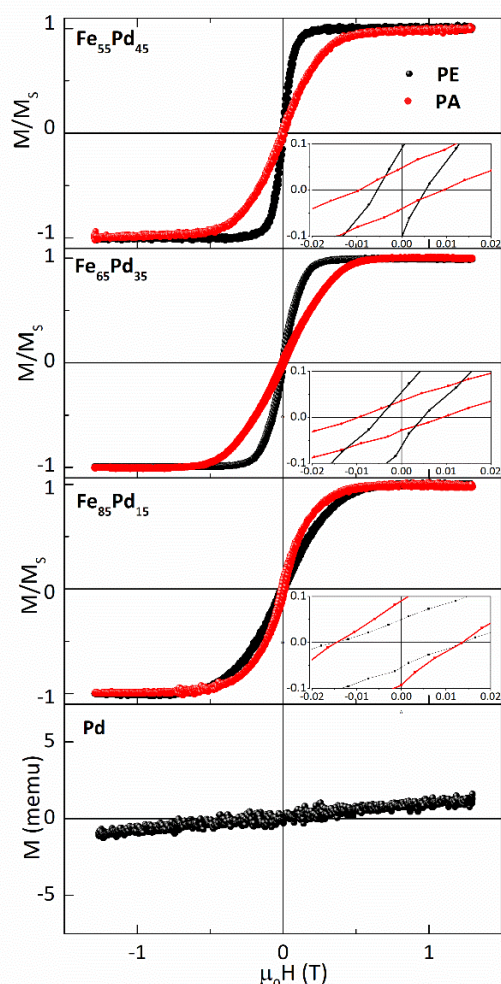
Figure 3. Hysteresis loops of Fe-containing NWs arrays measured parallel (PA) and perpendicular (PE) to the applied magnetic field. Insets: close-up of the low-field region. The bottom graph corresponds to pure Pd NWs, which display a paramagnetic behavior.

indicates that α-Fe and *fcc* Fe–Pd alloy phases coexist in this case.

Figure 3 shows the room temperature magnetic hysteresis loops corresponding to the different FePd NWs arrays ordered inside the AAO template. The normalized magnetic moment vs. magnetic field was measured with the applied magnetic field parallel (PA) and perpendicular (PE) to the NWs long axis. As it can be seen, the magnetic easy axis is along the NWs long axis, as expected when shape anisotropy is important. In sample $Fe_{85}Pd_{15}$ this effect is reduced possibly because of Fe segregation, as confirmed by XRD results.

All the Fe-containing samples exhibit soft magnetic behavior with modest coercivities of around 10 mT in both PA and PE configurations. Pecko *et al.* have obtained similar values of coercivity for $Fe_{55}Pd_{45}$ NWs with a diameter of 200 nm.[36,37] In every case, remanence is low in both configurations, resulting in a fast loss of magnetization when the external magnetic field is removed. Both in $Fe_{65}Pd_{35}$ and in $Fe_{55}Pd_{45}$ the response to the external field is faster when it is applied parallel to the NWs axis. In the case of Pd NWs, a paramagnetic behavior is observed, as expected for this element.

Figure 4 shows the survey spectrum of $Fe_{65}Pd_{35}$ NWs@βCDMOD14, which was acquired after etching the surface with an ion beam in order to eliminate the adsorbed βCDMOD14 molecules. The presence of Pd, Fe and some adventitious C are confirmed. Atomic % composition, calculated from this spectrum, confirms the results obtained by using EDS data (Table S1).
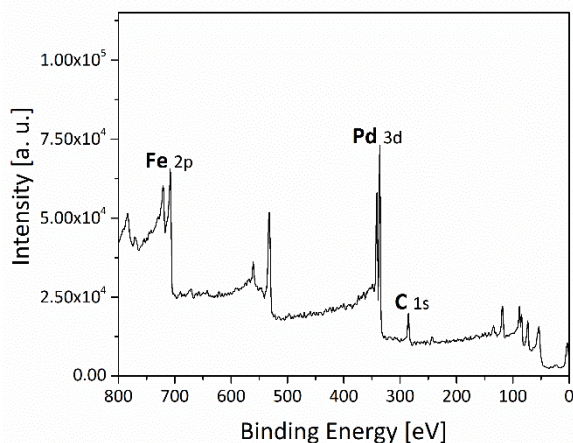

Figure 4. Survey spectrum of $Fe_{65}Pd_{35}$ NWs.
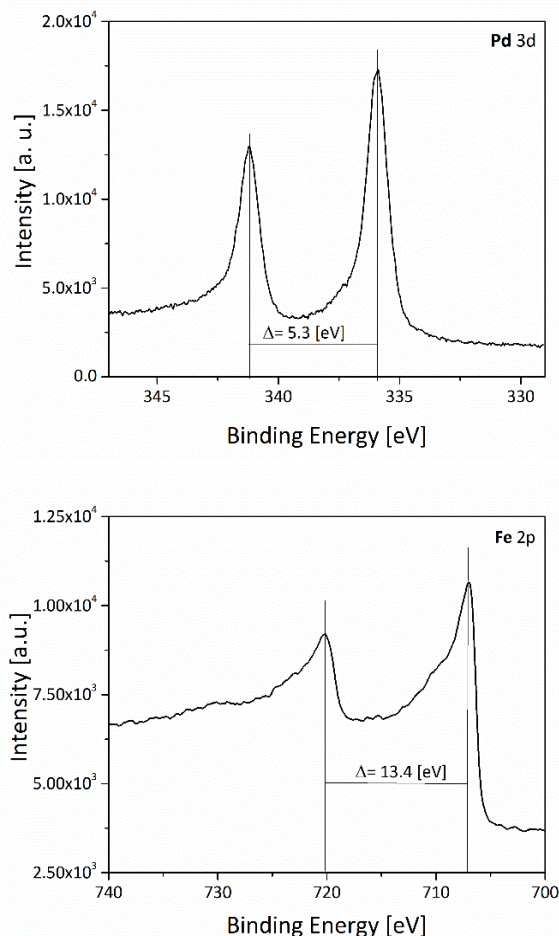
Figure 5 shows high-resolution spectra corresponding to Pd 3d

Figure 5. Full scan of $Fe_{65}Pd_{35}$ NWs high-resolution spectra for Pd 3d (top) and Fe 3p (bottom).

and Fe 2p signals from $Fe_{65}Pd_{35}$NWs after etching. The peaks' asymmetrical shape and the split of 5.3 eV between the peaks corresponding to Pd 3d 3/2 and 3d 5/2, as well as the split of 10.4 eV between Fe 2p 1/2 and 2p 3/2, confirm the presence of the metallic form of these species. Pd signal values were slightly shifted, in +0.9 eV: 335.9 eV and 341.2 eV (335.0 eV and 340.3 eV were expected) which has been reported as an effect of the compressive lattice strain in Pd by alloying with Fe. The signal values for Fe were 706.9 eV and 720.4 eV, as it was expected[17,38]

Catalytic studies. In order to evaluate the catalytic performances of Fe_xPd_{100-x} (x = 0, 55, 65, 85) NWs@βCDMOD14 (FePd NWs@βCDMOD14), the catalysts were used in the reduction of 4-NP under the presence of $NaBH_4$ in aqueous medium. The UV–vis spectra of the 4-NP and $NaBH_4$ mixture with FePd NWs@βCDMOD14 show a strong absorption peak around 400 nm, which is attributed to the formation of 4-NP$^-$ anion. This peak decreases as the reaction proceeds, and a band centered at 300 nm corresponding to the product 4-AP appears (Figure S2). The appearance of an isosbestic point at 314 nm indicates that

there is no accumulation of any reaction intermediate. All the results exposed in this section were obtained by using this reaction.

For the experimental conditions used in this work, we assumed: 1) the concentration of $NaBH_4$ does not change during the reaction due to its large excess with respect to 4-NP, thus the reduction rate constant (k_{obs}) was obtained by plotting $\ln(Abs_t/Abs_{t=0})$ versus time (t) measuring absorbance values at 400 nm, and 2) k_{obs} is proportional to the parameter
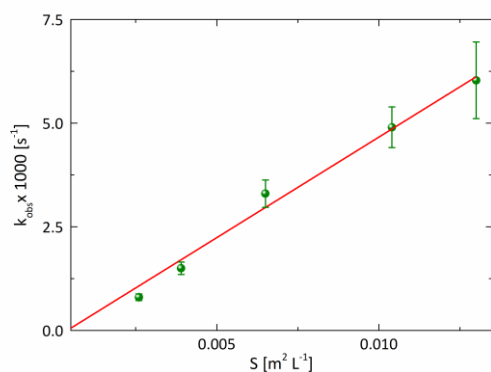
Figure 6. Surface dependence of k_{obs} as a function of the total surface S for $Fe_{55}Pd_{45}$ NWs@βCDMOD14, at $[NaBH_4]$ = 0.1 M.

S (the total surface) of all FePd NWs@βCDMOD14 in the systems, as plotted in Figure 6.

The parameter S was used to evaluate the dependence of k_{obs} on the catalysts area. S is defined as the catalyst area per unit volume of reaction medium and it is calculated from the catalyst's geometrical and physical parameters and the final volume of the reaction medium (see SI).

Hence, k_{obs} values are strictly proportional to the total surface of FePd NWs@βCDMOD14; the kinetic constants k_{obs} and S are related through Eq.1:

$$-\frac{d[4-NP]}{dt} = k_{obs}[4-NP] = k_1 S[4-NP] \qquad \text{Eq. 1}$$

where [4-NP] is 4-nitrophenol concentration, k_1 ($s^{-1}m^{-2}L$) is the rate surface constant and S (m^2L^{-1}) is the total surface area of
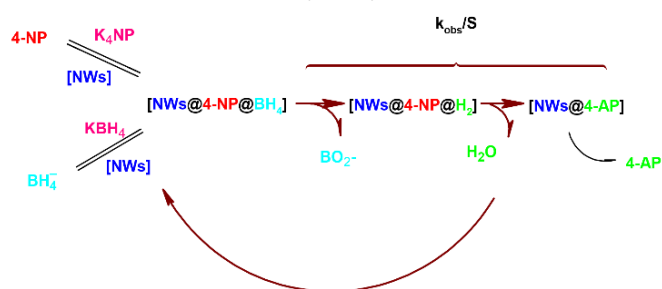
Scheme 2: Interactions and transformations taken into account in the reduction reaction of 4-NP in presence of $NaBH_4$ mediated by FePd NWs@βCDMOD14 (NWs in the scheme).

FePd NWs@βCDMOD14. In order to compare different catalysts, it is useful to calculate the ratio k_{obs}/S, since this quantity is independent from geometrical factors and the mass of catalyst used in the experiment. Scheme 2 is a representation of the interactions and transformations involved in the catalytic reduction of 4-NP on the NWs surface. Figure 7 shows the k_{obs}/S values obtained for catalysts of all compositions. It is clear from the graph that k_{obs}/S values are remarkably larger for $Fe_{55}Pd_{45}$ and $Fe_{65}Pd_{35}$ NWs@βCDMOD14 than for $Fe_{85}Pd_{15}$, and even pure Pd NWs@βCDMOD14. It is also worth mentioning that we examined the k_{obs} of bare NWs,
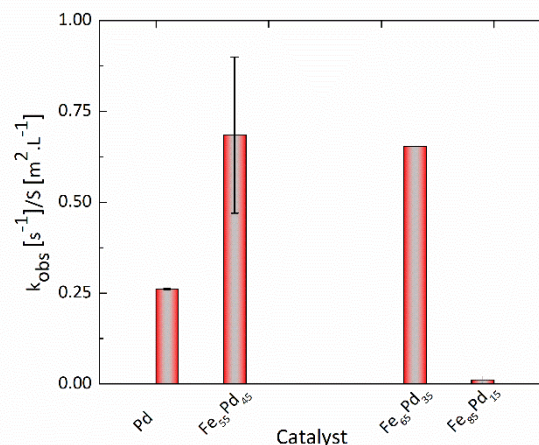
Figure 7. k_{obs}/S for all the studied FePd NWs@βCDMOD14. The reaction conditions were 10^{-4} M 4-NP, 0.1M $NaBH_4$ and 50 μL of catalyst solutions.

i.e. NWs without βCDMOD14 and we observed that k_{obs} values for these catalysts were about 10 times smaller than those obtained for FePd NWs@βCDMOD14. It is likely that the relatively poor catalytic properties of bare NWs are due to their low colloidal stability in water, in contrast with higher colloidal stability of FePd NWs@βCDMOD14.[29]

For a mechanistic analysis of the catalytic activity, we used the Langmuir–Hinshelwood model. Briefly, this model assumes that adsorption and desorption processes are fast and reversible, therefore the transfer of hydrogen or electrons occurs from NWs to 4-NP, producing 4-AP that it is then dissociated from the surface (See Scheme 2).

Since the reaction rate depends on the surface coverage by the reactants, 4-NP and BH_4^-, it can be rewritten as:

$$-\frac{d[4-NP]}{dt} = k_{obs}[4-NP] = k_1 S[4-NP] = kS\theta_{4-NP}\theta_{BH_4^-} \qquad \text{Eq. 2}$$

where k is the catalytic rate constant, ϑ_{4-NP} and ϑ_{BH4} correspond to the degree of surface coverage by 4-NP and BH_4^- respectively, and can be expressed using the Freundlich equilibrium isotherm shown in the SI, Eq. S1 and S2. Then, k_{obs} (Eq. (2)) can be rewritten as follows:

Eq. 3

$$k_{obs} = \frac{kS\theta_{4-NP}\theta_{BH_4^-}}{[4-NP]} = \frac{kSK_{4-NP}^n[4-NP]^{n-1}\left(K_{BH_4^-}\left[BH_4^-\right]\right)^m}{\left(1+\left(K_{4-NP}[4-NP]\right)^n+\left(K_{BH_4^-}\left[BH_4^-\right]^m\right)\right)^2}$$

where K_{4-NP} and K_{BH4} are the adsorption equilibrium constants of 4-NP and BH_4^-, respectively. The constants n and m are named Freundlich exponents and take into account the energetic surface heterogeneity; when $n=1$ and $m=1$ there is adsorption sites homogeneity, and the equilibrium can be well described by a Langmuir isotherm.

Figure 8 shows k_{obs} with variable concentrations of NaBH$_4$ in presence of Fe$_{55}$Pd$_{45}$ NWs@βCDMOD14. The values of k_{obs} increase with increasing concentration of NaBH$_4$ until they reach a maximum value at concentrations ~0.1 M NaBH$_4$, and then keep a constant value of k_{obs} =(0.009±0.001) s^{-1}. It was suggested that competitive adsorptions between 4-NP and BH$_4^-$ can influence the overall reaction rate and thus the reaction proceeds more quickly when the reactants' concentration is increased, until reaching the maximal rate. Afterwards, the reaction rate decreases because the defective reagent is displaced from the catalyst's surface.[39] We suggest that the plateau value for k_{obs} shown in Figure 8 is related to the active site saturation with molecular hydrogen. Given the fact that k_{obs} does not decrease after reaching the maximum value, this could indicate that 4-NP has a greater affinity for
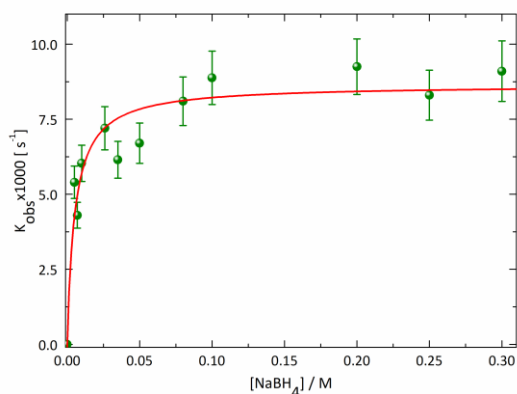
Figure 8. Plot of k$_{obs}$ vs. [NaBH$_4$] for the reduction reaction of 4-NP in presence of Fe$_{55}$Pd$_{45}$ NW@βCDMOD14. Solid line: fitting curve using Eq. (5), r$_2$=0.90 1.10^{-4}M 4-NP, 50 μL of catalyst solution.

the surface of Fe$_{55}$Pd$_{45}$ NWs@βCDMOD14 than for the reducing agent, and therefore, the latter is not able to move the 4-NP from active sites in the range of used NaBH$_4$ concentrations. It should be noted that the behavior of the other FePd alloys NWs was similar to that shown in Figure 8 (see Figure 3 SI).

Figure 9 shows the effect of 4-NP increasing concentration on k_{obs} while keeping NaBH$_4$ concentration constant ([NaBH$_4$] = 0.1 M). As it can be observed, increasing 4-NP concentration decreases the degradation rate. These results are attributed to the displacement of hydrogen molecules by 4-NP from the
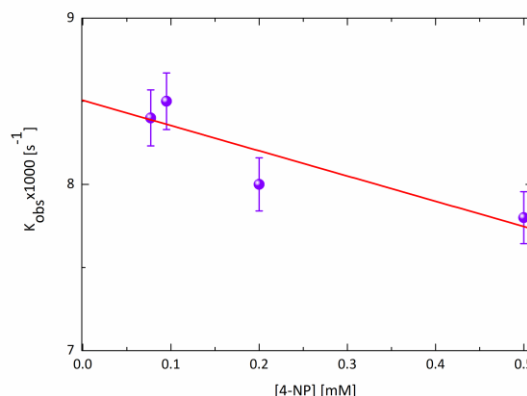
Figure 9. Plot of k$_{obs}$ vs. [4-NP] for the reduction reaction with [NaBH$_4$] = 0.1 M in presence of Fe$_{55}$Pd$_{45}$ NWs@CDMOD. Solid line: fitting curve using Eq. (4). r^2=0.71. 50 μL of catalyst solution.

active sites of Fe$_{55}$Pd$_{45}$ NWs@βCDMOD14, which agrees with reports from other authors.[34,39]

The kinetics data of Figure 8 (k_{obs} vs. [BH$_4^-$] plot) were fitted using the Langmuir–Hinshelwood model to obtain kinetic parameters and the best fit values were obtained if the Freundlich exponents were $n=1$ for 4-NP and $m=1$ for NaBH$_4$ and K_{4-NP} = 500 M^{-1}. These values are similar than those obtained in a previous work, using Pd NPs@βCDMOD14 instead of nanowires.[33] The fitting results corresponding to k and K_{BH4} are shown in Table 3. On the other hand, the experimental data shown in Figure 9 (k_{obs} vs. [4-NP] plot) are not well represented by Eq. (3), likely due to the small variation of k_{obs} values observed in the [4-NP] range used. Therefore, in this case, we fitted the kinetics data using a first-order Taylor series approximation to Eq. (4) (see SI for details of the Taylor series expansion) around the point [4-NP] = 0:

$$k_{obs} \approx k_{obs}\left([4-NP]=0\right)+\frac{\partial k_{obs}}{\partial[4-NP]}\left([4-NP]=0\right).[4-NP] \qquad \text{Eq. 4}$$

The slope of the linear approximation shown in Eq. (4) is described by the following expression:

$$\frac{\partial k_{obs}}{\partial[4-NP]}\left([4-NP]=0\right) = \frac{-2.k.S.\left(K_{4-NP}\right)^2.\left(K_{BH_4^-}\left[BH_4^-\right]\right)}{\left(1+\left(K_{BH_4^-}\left[BH_4^-\right]\right)\right)^3} = slope \qquad \text{Eq. 5}$$

We calculated K_{4-NP} for Fe$_{55}$Pd$_{45}$ NWs@βCDMOD14 using Eq. (5), the experimental slope (slope$_{Exp}$= -(1.5 ± 0.5 s^{-1} M^{-1})) from Figure 8, and the values corresponding to k, S and K_{BH4} are listed in Table 4, together with the values of K_{4-NP} estimated for all FePd NWs@βCDMOD14.

The values of K_{BH4} using FePd NWs@βCDMOD14 as catalysts are in the same order of those reported in the literature for Pd NPs@βCDMOD14 and other metallic NPs catalysts; however, we observe a slightly higher binding affinity for the catalysts containing 45% and 35% Pd.[30] These results show that BH$_4^-$ anion has a lower affinity for the metal surface than 4-NP, and although the active sites on the surface of FePd

NWs@βCDMOD14 become saturated with the reducing agent at [NaBH$_4$]= 0.1 M, they cannot displace 4-NP even if NaBH$_4$ concentration reaches a value of 0.3 M. The values of K_{4-NP} for FePd NWs@βCDMOD14 are in the same order of those reported previously for the constant of association of β-cyclodextrin with 4-NP in aqueous solution and Pd-NPs@CDMOD14, which suggests that the Taylor series provides a good approximation.[40–42] It seems that cyclodextrin as a ligand plays two important roles in the performance of the catalyst: 1) improving colloidal stability by avoiding agglomeration of the nanostructures, which gives a higher surface area of the catalyst and more active sites on the surface; and 2) increasing the surface concentration of 4-NP by providing a superficial anchor point for 4-NP and preventing its displacement once the surface of the catalyst is completely saturated with the reducing agent.

Table 3. Rate constants and adsorption constants of 4-NP and BH$_4$ and the total surface area per unit volume (S) of Fe$_x$Pd$_{100-x}$ (x = 0, 55, 65, 85) NWs@ βCDMOD14.

Catalyst	k [10^{-3} L M^{-1} s^{-1} m^{-2}] [a]	K_{NaBH4} [a]	K_{4-NP} [M^{-1}] [b]	S [10^{-3} m^{2}L^{-1}] [c]
Fe$_{85}$Pd$_{15}$	0.10±0.01	3±1	n.d.	21
Fe$_{65}$Pd$_{35}$	5.5±0.1	9±3	300±100	7
Fe$_{55}$Pd$_{45}$	6.3±0.5	10±2	300±100	14
Fe$_0$Pd$_{100}$	1.7±0.4	4±2	1000±300	7

k: catalytic rate constant. K4-NP and KBH4: adsorption constants of 4-NP and BH4- respectively   [a] A value of K4-NP=500 M-1 was kept fixed during the fitting of Eq. (5) to the kobs [BH4-] data.

[b] Values obtained from the linear approximation (Eq. 6).

[c] For calculation of S see Supplementary Information

n.d.: Not determined

We find that k values for Fe$_{55}$Pd$_{45}$ and Fe$_{65}$Pd$_{35}$ NWs@βCDMOD14 are 3-4 times greater than k values for Pd NWs@βCDMOD14, and 50-60 times greater than k values for Fe$_{85}$Pd$_{15}$, so it is clear that the presence of iron in a defined percentage in the structure is a favorable factor for the catalytic activity. A similar behavior was observed by others authors during the course of catalytic decomposition of NaBH$_4$ using trimetallic Ni$_x$Fe$_x$Pd$_{100-2x}$ (x = 25, 40, 45) catalyst.[43] They observed that alloys with a 50% Pd content have positive effects on the hydrogen generation rate. The synergistic effect was attributed to the fact that Pd facilitated H$_2$ activation and stabilization of metallic Fe. [44,45]

The synergistic effect was also found in other Fe$_2$O$_3$ catalysts promoted by Fe and the addition of Pd. Pd atoms activated the surface for H$_2$ adsorption, and Fe atoms adsorb and activate the substrate, m-cresol.[47] This seems a plausible explanation also for FePd NWs@βCDMOD14 because (1) *m*-cresol and 4-

NP have structural similarities (both can interact with Fe active in the same manner), and (2) it was proposed that during reduction reaction of 4-NP it is H$_2$ rather than borohydride the reducing agent, therefore the variation in Pd content namely 35% < Pd < 45% of FePd NWs@βCDMOD14 could result in the increase of H$_2$ selectivity, as it was reported in other systems.[23,24]

It has also been proposed by other authors that electron-enriched metal active sites are necessary to facilitate the catalysis reaction and these electrons are provided by the alloying of Pd to the active metal sites.[23,24] The shift observed in the valence band of Pd 3d XPS spectra (Figure 5) for Fe$_{65}$Pd$_{35}$ NWs@βCDMOD14 suggests that the charge transfer between the constituent elements is appreciable upon alloy formation.[48] The same trend has been reported by other researchers, who have observed a positive shift with respect to pure Pd when the Pd–Fe alloy is formed and show that the alloying Fe atoms increase the electrocatalytic performance of the Pd–Fe catalyst for oxygen reduction, which may be attributed to the change in the electronic structure of Pd atoms, Pd–Pd bond length and surface composition of Pd in Pd–Fe/C catalysts. [49–51]

As it has been reported, H is preferentially adsorbed on FePd *fcc* (and *fct*) alloys;[23–25] this could explain that samples Fe$_{65}$Pd$_{35}$ and Fe$_{55}$Pd$_{45}$, which are rich in the *fcc* phase, are the ones with the highest catalytic activity. Briefly, the authors explained that hydrogen is adsorbed and stored in the interstitial sites of these alloys, but when the hydrogen adsorption is above 10% it reacts to form mainly reversible hydrides, thus it was proposed for hydrogen storage. Furthermore, it has been shown that the energy gain when H is located in the Pd–Fe sites is greater than when it is positioned in the interstices of pure Fe or Pd. In addition, the H atoms that enter the interstitial sites form intermetallic hydrides, which prevent oxidation.[49]

It is evident that particular Pd-Fe alloys have Pd and Fe modified electronic structures that seem appropriate for catalysis. As it has been reported by several spectroscopic and computational investigations, the catalytic performance of bimetallic catalysts is strongly dependent on the coordination environment of the active sites.[52,53] For instance, Pd-Au bimetallic nanoparticles (with Au/Pd ratios of ~40 and greater) expose isolated atoms (i.e. monomers) and oligomeric Pd atoms on the nanoparticles surfaces which provide selective stabilization of transition states for H$_2$O$_2$ during catalytic reduction of O$_2$ to H$_2$O$_2$[54,55]

Finally, from the comparison between k values for Pd NWs@βCDMOD14 catalyst and the value k ~1.50 x 10^{-3} L s^{-1}m^{-2} obtained for Pd NPs@βCDMOD14,[30] it is possible to highlight the importance of the use of the parameter *S* in order to obtain catalytic constants that are independent from the quantity and morphology of the catalyst used.

Recovery test. An important advantage of using FePd NWs@βCDMOD14 as catalysts is the ease of recovery from the reaction mixture and reusability of the Pd-containing

nanocatalyst. Upon completion of the reaction, the magnetic properties of the FePd NWs@βCDMOD14 provide a straightforward way to isolate the catalyst from the colloidal solution with the simple application of an external magnetic field, as shown in Figure 10A, which displays a photograph of FePd NWs@βCDMOD14 attracted by a magnet. In Figure 10B the k_{obs} (recovered NWs) / k_{obs} (fresh NWs) ratio is shown. The results indicate that the recovered $Fe_{55}Pd_{45}$ NWs@βCDMOD14 catalysts lost almost 70% of their initial activity after washing with water or diluted acid solution, however the loss of activity is less than 20 % after washing with βCDMOD14 alkaline solution ([βCDMOD14]= 5.10^{-4}M, pH=9). This latter result is consistent with the above-mentioned role of cyclodextrins in the catalyst performance and it seems that some βCDMOD14 attached to the NWs surface is partly lost during the catalyst recycling. This can be restored by recycling with the addition of fresh βCDMOD14 alkaline solution. The catalyst can be recycled at least 3 times without losing its catalytic capacity.
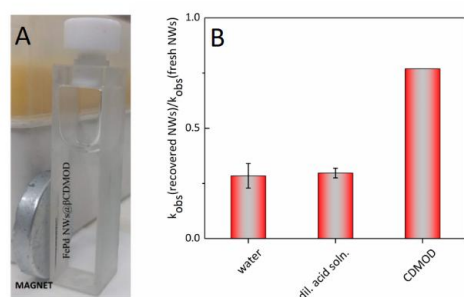
Figure 10. A. Photograph of a magnet attracting FePd@βCDMOD14 NWs from the solution. **B.** k_{obs} recovered NWs / k_{obs} fresh NWs after washing with water, diluted acid solution and a solution of βCDMOD14 ([βCDMOD14]= 5.10^{-4}M pH=9). A fresh solution of catalyst was used as reference.

Conclusions

FePd nanowires with different compositions have been synthesized through a simple electrodeposition technique using AAO as templates, by changing the composition of the electrolyte. All Fe-Pd nanowires are ferromagnetic in the entire explored composition range and XRD analysis revealed that $Fe_{55}Pd_{45}$ and $Fe_{65}Pd_{35}$ NWs are single-phase binary alloys with a disordered face centered cubic (*fcc*) crystalline structure. After surface modification using amphiphilic cyclodextrins, the colloidal stability of NWs@βCDMOD14 in water was improved and they were used as catalysts for reduction of 4-NP in presence of $NaBH_4$ in aqueous medium.

$Fe_{55}Pd_{45}$ and $Fe_{65}Pd_{35}$ NWs@βCDMOD14 showed the highest catalytic performance, which was attributed to the presence of the *fcc* single-phase that improved the H-metal interaction at the interfaces. This crystalline phase has a high H_2 selectivity, which is the reducing reagent generated in situ on the metal surface, probably due to the increasing of electron-enriched metal active sites upon the alloy. So, the alloy composition with ~35% Pd results optimal for the studied reaction.

The possibility of recycling and reusing the material in consecutive catalytic cycles demonstrated that its initial activity still remains up to 80% after the third cycle. We believe that this relatively low-cost and recyclable catalytic system will promote new opportunities in the development of high-performance metal alloy catalysts.

Experimental

Materials and methods

NWs synthesis and characterization. NWs of different Fe/Pd compositions were prepared by template-assisted electrodeposition, using electrolytic baths of different Fe^{3+} and Pd^{2+} concentrations, (see Table 1) into the pores (200 nm diameter) of an anodic aluminium oxide (AAO) membrane.[29] The support electrolyte used was ammonium citrate, as the citrate complexes with Fe^{3+}, and it is therefore stable at high pH values. Ammonium hydroxide was added to the solution, to keep the pH = 9.00, thus ensuring the presence of ammonium ions that form a complex with Pd^{2+}. Prior to using as a template, a conductive thin gold layer was sputtered on one side of the membrane to be used as a cathode. A potential of -1.5 V was applied during 30 minutes for the electrodeposition in all cases. The chemical compositions of the resulting FePd NWs were determined by averaging several EDS spectra, taken after dissolving the alumina template (Figure 1 SI). The NWs morphology was observed in a Sigma Zeiss Field Emission Scanning Electron Microscope (FE-SEM). Crystalline phases were determined by X-ray diffraction (XRD) in a PANalytical Empyrean diffractometer using Cu Kα radiation (λ= 1.5418 Å) in the 2θ range from 30° to 90°. XPS experiments were carried out using a K-Alpha X-ray photoelectron spectroscope (Thermo-Fisher Scientific Co.) with a monochromatized Al-*K*α X-ray source in vacuum (10^{-9} mBar). All the magnetic measurements were carried out at room temperature in a Lakeshore 7300 vibrating-sample magnetometer (VSM), with a maximum magnetic field of ±1.3 T, applied both parallel (PA) and perpendicular (PE) to the NWs major axis.

Catalyst preparation. In order to free the NWs from the alumina template, they were immersed in a 0.1 M NaOH solution for 6 h. Then, after rinsing twice the NWs with ultra-pure water, 1 mL of a 5.10^{-4} M βCDMOD14 solution at pH 9.0 was added, and the NWs were kept in these conditions for 24 h. After that, the NWs were separated from the βCDMOD14 solution by rinsing several times to remove the βCDMOD14 excess. For the washing process, the NWs@βCDMOD14 were retained with a magnet, eliminating the remaining liquid.

Later, 2 mL of ultra-pure water was added. The so-obtained solution is henceforth called `catalyst solution'. The adsorption of βCDMOD14 on the NWs surface was assumed due to the high colloidal stability of the NWs after treatment with the βCDMOD14 and based on a previous work in which, following the same experimental procedure, the adsorption of βCDMOD14 on the surface of $Fe_{55}Pd_{45}$ NWs was confirmed by IR-ATR and XPS.[29]

Reduction reaction mediated by NWs. To study the reduction reaction, 0.3 mL of a 1 M $NaBH_4$ stock solution was added into 2.5 mL of water, 25 µL of 1.10^{-4} M 4-NP and 50µL of catalyst solution in an UV-vis quartz cell. Under the reaction conditions, 4-nitrophenolate (4-NP⁻) is the predominant species, so the absorbance changes were measured at its absorption maximum of 400 nm every 2 seconds. In order to be able to observe the effect of the reagents and the different catalysts on the reaction kinetics, different series of experiments were carried out varying the concentration of $NaBH_4$, 4-NP and the volume of catalyst solution used.

Conflicts of interest

There are no conflicts to declare.

Acknowledgements

Notes and references

1   V. R. Stamenkovic, B. Fowler, B. S. Mun, G. Wang, P. N. Ross, C. A. Lucas and N. M. Markovic, *Science (80-.).*, 2007, **315**, 493–497.

2   L. Ou, *J. Chem.*, 2015, **2015**, 1–11.

3   L. Li, L.-X. Zhang, J.-L. Shi, J.-N. Yan and J. Liang, *Appl. Catal. A Gen.*, 2005, **283**, 85–89.

4   A. Tomer, B. T. Kusema, J. F. Paul, C. Przybylski, E. Monflier, M. Pera-Titus and A. Ponchel, *J. Catal.*, 2018, **368**, 172–189.

5   Q. Ma, N. Wang, G. Liu and L. Wang, *Microporous Mesoporous Mater.*, 2019, **279**, 245–251.

6   G. Chakraborty, I. H. Park, R. Medishetty and J. J. Vittal, *Chem. Rev.*, 2021, **121**, 3751–3891.

7   M. Yamauchi, R. Ikeda, H. Kitagawa and M. Takata, *J. Phys. Chem. C*, 2008, **112**, 3294–3299.

8   F. Amaladasse, A. Gupta, S. Shervani, S. Sivakumar, K. Balani and A. Subramaniam, *Part. Sci. Technol.*, 2020, **0**, 1–7.

9   T. A. Revathy, S. Dhanavel, T. Sivaranjani, V. Narayanan, T. Maiyalagan and A. Stephen, *Appl. Surf. Sci.*, 2018, **449**, 764–771.

10   L. Kuai, Z. Chen, S. Liu, E. Kan, N. Yu, Y. Ren, C. Fang, X. Li, Y. Li and B. Geng, *Nat. Commun.*, 2020, **11**, 1–9.

11   Palladium: The Secret Weapon in Fighting Pollution, https://www.visualcapitalist.com/palladium-the-secret-weapon-in-fighting-pollution/, (accessed 26 May 2021).

12   J. Kielhorn, C. Melber, D. Keller and I. Mangelsdorf, *Int. J. Hyg. Environ. Health*, 2002, **205**, 417–432.

13   G. Schertzinger, S. Zimmermann, D. Grabner and B. Sures, *Environ. Pollut.*, 2017, **230**, 31–39.

14   M. Akkoç, N. Buğday, S. Altın, N. Kiraz, S. Yaşar and İ. Özdemir, *J. Organomet. Chem.*, 2021, **943**, 1–10.

15   L. Strimbu, J. Liu and A. E. Kaifer, *Langmuir*, 2003, **19**, 483–485.

16   S. Yamamoto, S. Takao, S. Muraishi, C. Xu and M. Taya, *Mater. Chem. Phys.*, 2019, **234**, 237–244.

17   D. Liu, Q. Zeng, H. Liu, C. Hu, D. Chen, L. Xu and J. Yang, *Cell Reports Phys. Sci.*, 2021, **2**, 100357.

18   J. Li and S. Sun, *Acc. Chem. Res.*, 2019, **52**, 2015–2025.

19   J. Liu, C. Q. Sun and W. Zhu, *Electrochim. Acta*, 2018, **282**, 680–686.

20   G. Jiang, X. Li, X. Lv and L. Chen, *Sci. Bull.*, 2016, **61**, 1248–1254.

21   G. Jiang, H. Zhu, X. Zhang, B. Shen, L. Wu, S. Zhang, G. Lu, Z. Wu and S. Sun, *ACS Nano*, 2015, **9**, 11014–11022.

22   Y. Yan, J. S. Du, K. D. Gilroy, D. Yang, Y. Xia and H. Zhang, *Adv. Mater.*, 2017, **29**, 1605997.

23   S. Ardenghi, E. González, P. Jasen and A. Juan, *Phys. Scr.*, 2009, **79**, 045702.

24   M. G. Ganchenkova, V. A. Borodin, S. Y. Binyukova, E. A. Gonzalez, P. V. Jasen and A. Juan, *Inorg. Mater. Appl. Res.*, 2011, **2**, 172–175.

25   P. V. Jasen, E. A. Gonzalez, N. J. Castellani and A. Juan, *Phys. Rev. B - Condens. Matter Mater. Phys.*, 2005, **71**, 1–7.

26   J. S. Riva, G. Pozo-López, A. M. Condó, M. S. Viqueira, S. E. Urreta, D. R. Cornejo and L. M. Fabietti, *J. Alloys Compd.*, 2016, **688**, 804–813.

27   J. S. Riva, A. V. Juárez, S. E. Urreta and L. M. Yudi, *Electrochim. Acta*, 2019, **298**, 379–388.

28   S. Noël, B. Léger, A. Ponchel, S. Sadjadi and E. Monflier, *Environ. Chem. Lett.*, 2021, **19**, 4327–4348.

29   E. Herrera, M. S. Aprea, J. S. Riva, O. F. Silva, P. G. Bercoff and A. Granados, *Appl. Surf. Sci.*, 2020, **529**, 2–7.

30   A. Cocq, B. Léger, S. Noël, H. Bricout, F. Djedaïni-Pilard, S. Tilloy and E. Monflier, *ChemCatChem*, 2020, **12**, 1013–1018.

31   Á. Molnár, *ChemCatChem*, 2021, **13**, 1424–1474.

32   O. F. Silva, M. A. Fernández, S. L. Pennies, R. R. Gil and R. H. De Rossi, *Langmuir*, 2008, **24**, 3718–3726.

33   M. V. Bravo, O. F. Silva, C. Adam and A. M. Granados, *J. Mol. Liq.*, 2020, **304**, 112725.

34   S. Gu, S. Wunder, Y. Lu, M. Ballauff, R. Fenger, K. Rademann, B. Jaquet and A. Zaccone, *J. Phys. Chem. C*, 2014, **118**, 18618–18625.

35   X. L. Fei, S. L. Tang, R. L. Wang, H. L. Su and Y. W. Du, *Solid State Commun.*, 2007, **141**, 25–28.

36   N. Ertugrul, R. Hasegawa, W. L. Soong, J. Gayler, S. Kloeden and S. Kahourzade, *IEEE Trans. Magn.*, 2015, **51**, 1–10.
37   D. Pečko, K. Ž. Rožman, N. Kostevšek, M. Shahid Arshad, B. Markoli, Z. Samardžija and S. Kobe, *J. Alloys Compd.*, 2014, **605**, 71–79.
38   M. P. Felicissimo, O. N. Martyanov, T. Risse and H. J. Freund, *Surf. Sci.*, 2007, **601**, 2105–2116.
39   S. Wunder, F. Polzer, Y. Lu, Y. Mei and M. Ballauff, *J. Phys. Chem. C*, 2010, **114**, 8814–8820.
40   J. Tang, Z. Shi, R. M. Berry and K. C. Tam, *Ind. Eng. Chem. Res.*, 2015, **54**, 3299–3308.
41   S. F. L. andRobert K. P. Jianjia Liu, Jie Wang, Zhongming Zhu, Li Li, Xuhong Guo, *AIChE J.*, 2014, **59**, 215–228.
42   M. V Rekharsky and Y. Inoue, *Chem. Rev.*, 1998, **98**, 1875–1917.
43   K. S. Al-Thubaiti and Z. Khan, *Int. J. Hydrogen Energy*, 2020, **45**, 13960–13974.
44   X. Song, P. Yang, J. Wang, X. Zhao, Y. Zhou, Y. Li and L. Yang, *Inorg. Chem. Front.*, 2019, **6**, 2727–2735.
45   D. Bhattacharjee and S. Dasgupta, *J. Mater. Chem. A*, 2015, **3**, 24371–24378.
46   X. Yang, H. Li, R. Ahuja, T. Kang and W. Luo, *Sci. Rep.*, 2017, **7**, 1–6.
47   Y. Hong, H. Zhang, J. Sun, K. M. Ayman, A. J. R. Hensley, M. Gu, M. H. Engelhard, J. S. McEwen and Y. Wang, *ACS Catal.*, 2014, **4**, 3335–3345.
48   S. L. Zhang and J. R. Zhang, *Phys. Status Solidi*, 1994, **182**, 421–427.
49   M. N. Al-Hinai, R. Hassanien, N. G. Wright, A. B. Horsfall, A. Houlton and B. R. Horrocks, *Faraday Discuss.*, 2013, **164**, 71–91.
50   Y. Tang, S. Cao, Y. Chen, T. Lu, Y. Zhou, L. Lu and J. Bao, *Appl. Surf. Sci.*, 2010, **256**, 4196–4200.
51   A. A. Shesterkina, L. M. Kustov, A. A. Strekalova and V. B. Kazansky, *Catal. Sci. Technol.*, 2020, **10**, 3160–3174.
52   B. Singh, M. B. Gawande, A. D. Kute, R. S. Varma, P. Fornasiero, P. McNeice, R. V. Jagadeesh, M. Beller and R. Zbořil, *Chem. Rev.*, 2021, **121**, 13620–13697.
53   L. Zhang, Y. Ren, W. Liu, A. Wang and T. Zhang, *Natl. Sci. Rev.*, 2018, **5**, 653–672.
54   T. Ricciardulli, S. Gorthy, J. S. Adams, C. Thompson, A. M. Karim, M. Neurock and D. W. Flaherty, *J. Am. Chem. Soc.*, 2021, **143**, 5445–5464.
55   T. Wang, A. Chutia, D. J. L. Brett, P. R. Shearing, G. He, G. Chai and I. P. Parkin, *Energy Environ. Sci.*, 2021, **14**, 2639–2669.

ARTICLE

TOC
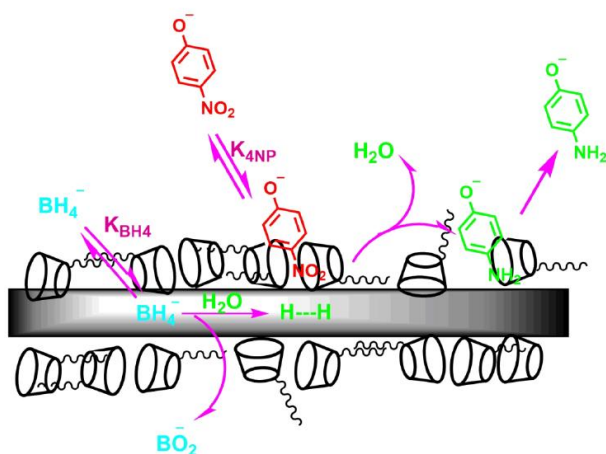
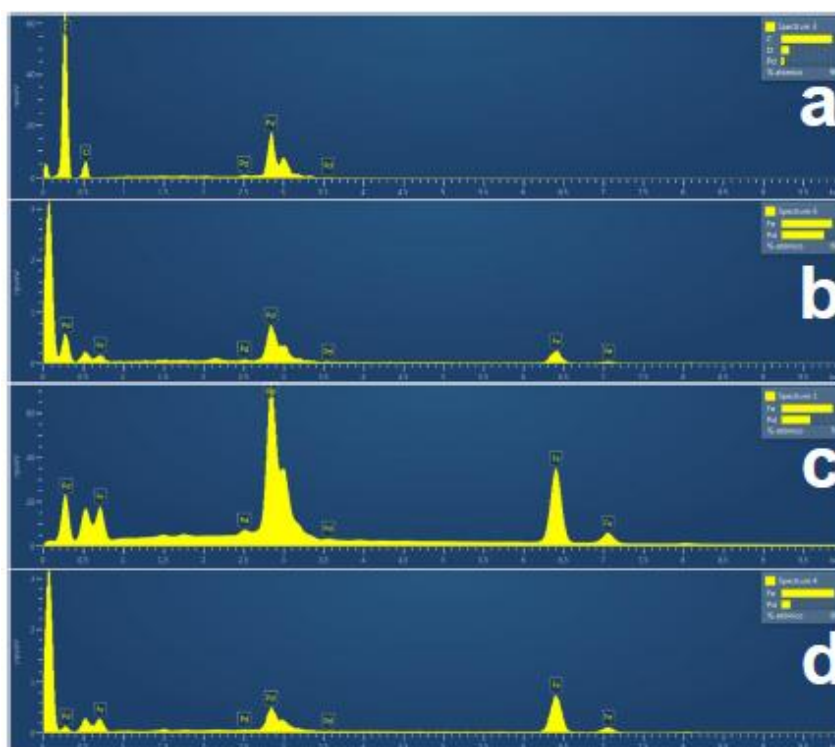**Supplementary Information**

1. Energy Dispersive X-Ray Spectroscopy

Figure S1. EDS spectra for FePd NWs of different composition. a) Pd b) Fe$_{36}$Pd$_{64}$ c) Fe$_{66}$Pd$_{34}$ d) and e) Fe$_{89}$Pd$_{11}$.

Table S1. Atomic % composition, calculated from XPS data.

Element	Atomic%	Atomic%[a]
C	15.9	
Pd	30.0	35.6
Fe	54.1	64.4

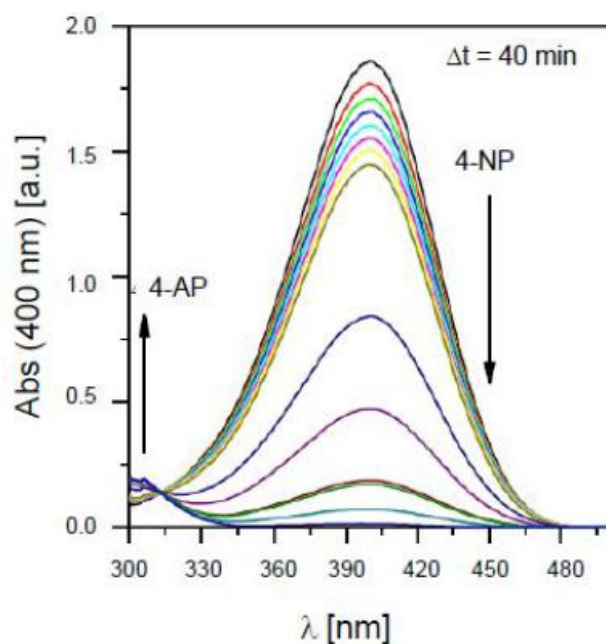[a] atomic % recalculated without considering C.

2. UV.vis measurements

Figure S2. UV-vis spectra at different times of the reduction reaction of 4-NP 10-4 M in aqueous solution containing NaBH4 0.1 M and FePd NWs@βCDMOD14
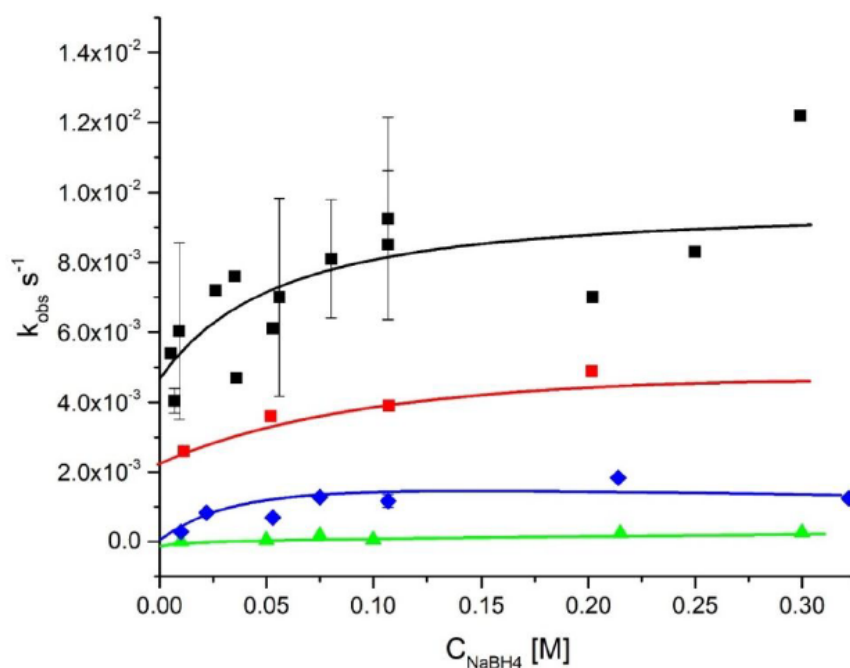
3. Catalytic studies

Figure S3.kobsvs [NaBH4] for reaction of 4-NP in presence of different alloys FePdNW@βCDMOD14. Fe55Pd45 (black line), Fe65Pd35 (red line), Pd (blue line) and Fe85Pd15 (green line).

$$\theta_{4-NP} = \frac{(K_{4-NP}[4-NP])^n}{1+(K_{4-NP}[4-NP])^n+\left(K_{BH_4^-}[BH_4^-]\right)^m} \qquad \text{Eq. S1}$$

$$\theta_{BH_4^-} = \frac{\left(K_{BH_4^-}[BH_4^-]\right)^m}{1+(K_{4-NP}[4-NP])^n+\left(K_{BH_4^-}[BH_4^-]\right)^m} \qquad \text{Eq. S2}$$

3.a. The Taylor series expansion

The deduction of formula (Eq. 6) is as follows: According Eq. 5, we consider that kobs is a function of [4-NP] variable and descripted by a rational function, $\frac{f}{g}$, Eq.S3:

$$k_{obs} = \frac{f}{g} = \frac{kSK_{4-NP}K_{BH_4^-}\left[BH_4^-\right]}{\left(1+K_{4-NP}[4-NP]+K_{BH_4^-}\left[BH_4^-\right]\right)^2} \qquad \text{Eq.S3}$$

Where f and g are described by Eq. S4 and Eq.S5 respectively,

$$f = \left(kSK_{4-NP}K_{BH_4^-}\left[BH_4^-\right]\right) \qquad \text{Eq.S4}$$

$$g = \left(1+K_{4-NP}\left[4-NP\right]+K_{BH_4^-}\left[BH_4^-\right]\right)^2 \qquad \text{Eq.S5}$$

We use the Taylor expansion around [4-NP]=0 to obtain a linear approximation of Eq.S3 by truncating at the first-order (Eq. S6)

$$k_{obs} \approx k_{obs}(0)+\frac{\partial k_{obs}}{\partial[4-NP]}(0).[4-NP] \qquad \text{Eq. S6}$$

Where the first derivate ($\frac{\partial k_{obs}}{\partial[4-NP]}$) was obtained through the derivatives of rational function and according to the following rule (Eq.S7):

$$\frac{\partial k_{obs}}{\partial[4-NP]} = \frac{f'.g - f.g'}{g^2} \qquad \text{Eq.S7}$$

Where f' and g' are the derivates of f and g respectively and described by Eq. S8 and Eq. S9

$$f' = 0 \qquad \text{Eq. S8}$$

$$g' = 2.K_{4-NP}.\left(1+K_{4-NP}\left[4-NP\right]+K_{BH_4^-}\left[BH_4^-\right]\right) \qquad \text{Eq. S9}$$

If we substitute Eq. S4, S5, S8 and S9 into Eq. (S7) evaluated at [4-NP]=0, we obtained the slope of the linear approximation of Eq. S6 which is descripted by Eq. S10

Eq.S10

$$\frac{\partial k_{obs}}{\partial [4-NP]}(0) = \frac{-2.k.S.(K_{4-NP})^2 \cdot (K_{BH_4^-}[BH_4^-])}{(1+(K_{BH_4^-}[BH_4^-]))^3} = slope$$

3.b. Determination of S

The theoretical value of S (the total surface area of FePdNWs normalized to the solution's unit volume) was determined through the following equations. Geometrical parameters of cylindrical NWs (length and diameter), were obtained experimentally (see Table S1).

$$S_{NW} = 2\pi r h + 2\pi r^2 \qquad\qquad V_{NW} = \pi r^2 h$$

$$\rho_{Pd^\circ} = 12.02 \cdot 10^3 \frac{kg}{m^3} \qquad\qquad \rho_{Fe^\circ} = 7.85 \cdot 10^3 \frac{kg}{m^3}$$

$PM_{Pd^\circ} = 106.42$ g/mol $PM_{Fe^\circ} = 55.84$ g/mol

Where r=100nm is the NW radius, and L is their length (values in table S1), V_{NW} and S_{NW} are the volume and the surface of each individual NW, respectively, ρPd and ρFe are the density of Pd^0 and Fe^0, respectively, $PM\ Pd^0$ and $PM\ Fe^0$ are the molar mass of Pd^0 and Fe^0, respectively.

The density of each FePdNW composition ($\rho Fe_{(100-x)}Pd_x$), the individual mass (m_{NW}), the total quantity (N), the individual surface (S_{NW}) and the surface in 'catalyst solution' ($S'cs'$) were calculated by using the follow equation and values obtained informed in Table S1.

$$\rho_{Fe_{(100-x)}Pd_x} = \frac{[\rho_{Fe} \cdot (100-x)] + [\rho_{Pd} \cdot x]}{100}$$

$$m_{NW} = \rho_{Fe_{(100-x)}Pd_x} \cdot V_{NW} \qquad \text{(see Sec. 2.2)}$$

$$S'_{cs'} = N \cdot S_{NW}/2.10^{-3}L$$

$$N = m_{NW}/m_{sample}$$

$$S'_{cs'} = S_{NW}/2 \cdot 10^{-3}$$ Finally, S is the total surface which takes in account the dilution factor (50µL of NWs in 2.8mL)

Table S2: Geometrical parameters and constants for the different NWs alloys

Composition [at%]	Length La [±2 µm]	V_{NW} [$10^{-20}m^3$]	ρ [10^3 kg/m^3]	m_{NW} [10^{-12} g]	m [mg]	N [10^8]	S_{NW} [10^{-12} m^2]	S [10^{-3}m^2 L^{-1}]
Fe85Pd15	8	25.1	7.85	1.97	1.0±0.1	5.1	5.1	21
Fe65Pd35	22	69.1	9.31	6.43	0.4±0.1	0.6	13.9	7
Fe55Pd45	13	40.8	9.73	3.97	0.8±0.1	2.0	8.2	14
Fe0Pd100	10	31.4	12.02	3.78	0.5±0.1	1.3	6.3	7

.